npj computational materials

www.nature.com/npjcompumats

ARTICLE OPEN

Check for updates

Peculiar band geometry induced giant shift current in ferroelectric SnTe monolayer

Gan Jin[1,2] and Lixin He[1,2,3]✉

The bulk photovoltaic effect (BPVE) occurs when homogeneous noncentrosymmetric materials generate photocurrent or photovoltage under illumination. The intrinsic contribution to this effect is known as the shift current effect. We calculate the shift current conductivities of the ferroelectric SnTe monolayer using first-principles methods. Our results reveal a giant shift-current conductivity near the valley points in the SnTe monolayer. More remarkably, the linear optical absorption coefficient at this energy is very small, resulting in an enormous Glass coefficient that is four orders of magnitude larger than that of $BaTiO_3$. To understand these giant shift-current effects, we employ a three-band model and find that they arise from the nontrivial energy band geometries near the valley points, where the shift-vector diverges. This serves as a prominent example highlighting the crucial role of band geometry in determining the fundamental properties of solids.

npj Computational Materials (2024)10:23 ; https://doi.org/10.1038/s41524-024-01213-w

INTRODUCTION

The study of bulk photovoltaic effect (BPVE) has a long history[1–3], and recently it has attracted great renewed interest because it potentially allows the energy conversion efficiency to surpass the Shockley-Queisser limit[4,5]. The shift-current effects are believed to be the primary intrinsic contribution to the BPVE[3,6]. They offer an alternative to the photocurrent generated by traditional semiconductor p-n junctions[7,8]. It has been demonstrated that the photovoltage generated by shift-current effects can far exceed the band gap[9–12].

The high priority of current studies in the field is to discover materials that have high shift-current conductivities. Cook et al. proposed principles for designing shift current materials using an effective two-dimensional model and successfully applied them to the monochalcogenide GeS[8]. In addition to conventional ferroelectric materials[13,14], special attention has been given to Weyl semimetals because of the special topological nature of their band structures[15,16]. Ahn et al.[17] theoretically studied the low-frequency properties of BPVEs in topological semi-metals and revealed the relationship between the shift current, injection current, and the quantum geometry of the material near the Weyl point. Recent studies[18–20] indicate a significant potential for substantial nonlinear optical responses in layered two-dimensional materials, including BPVE and second harmonic generation.

In this work, we investigate the nonlinear optical properties of the two-dimensional ferroelectric material SnTe monolayer[21] using first-principles methods. We find that it has giant shift current conductivities near the valley points. More remarkably, the linear optical absorption coefficient at this energy is very small, which leads to an enormous Glass coefficient of four orders of magnitude larger than that of bulk $BaTiO_3$[1,5,22]. We develop a minimal three-band model to analyze the mechanism of the giant shift-current effect in the SnTe monolayer. We find that the giant shift-current effects are induced by the nontrivial band structure geometry, where the shift-vector diverges at the valley point. We further show that the giant shift-current is related to the derivatives of the imaginary part of the quantum geometric tensor near the point. The mechanism is different from the previous works on the Weyl semimetals[17], and therefore opens a play ground for the fascinating physical properties that are determined by the band structure geometries.

RESULTS

Crystal structure

In 2016, Chang et al.[21] reported that the SnTe monolayer exhibits robust in-plane ferroelectricity with a Curie temperature of up to 270 K, which is significantly higher than its bulk counterpart at 98 K. The SnTe monolayer has a hinge-like structure similar to that of phosphorene, as shown in Fig. 1, and belongs to the $Pmn2_1$ space group with mirror (M_{xz}) and glide mirror (G) symmetries. The in-plane ferroelectricity of the SnTe monolayer is oriented along the x-axis[23–26]. Due to its lack of inversion symmetry, the SnTe monolayer is expected to exhibit shift-current effects.

Band structure and shift current conductivities

We perform first-principles calculations to investigate the shift-current effects in the SnTe monolayer. Details of the calculations are presented in the METHODS section.

The band structures of SnTe monolayer with and without spin-orbit coupling (SOC) are shown in Supplementary Fig. 1. There are four valley points of the band structure in the first Brillouin zone. Two valley points, $\mathbf{k}_0 = (0.416, 0.0)$, $\mathbf{k}_1 = (0.0, 0.415)$, are situated on the $\Gamma - X$ line and $\Gamma - Y$ line, respectively, in direct coordinates. The other two valley points are obtained by the time inversion symmetry of the aforementioned two k-points, namely $\bar{\mathbf{k}}_0 = -\mathbf{k}_0$ and $\bar{\mathbf{k}}_1 = -\mathbf{k}_1$, as displayed in Fig. 1d. The band gaps at points $\mathbf{k}_0$ ($\bar{\mathbf{k}}_0$) and $\mathbf{k}_1$ ($\bar{\mathbf{k}}_1$) are 1.21 eV and 1.45 eV, respectively. The positions of the valley points are only slightly altered upon the introduction of SOC, as shown in Supplementary Fig. 1.

The lack of inversion symmetry in the SnTe monolayer results in a shift current, which is a nonlinear dc photocurrent induced by

[1]Key Laboratory of Quantum Information, University of Science and Technology of China, Hefei 230026, China. [2]Hefei National Laboratory, University of Science and Technology of China, Hefei, Anhui 230088, China. [3]Institute of Artificial Intelligence, Hefei Comprehensive National Science Center, Hefei, Anhui 230026, China. ✉email: helx@ustc.edu.cn

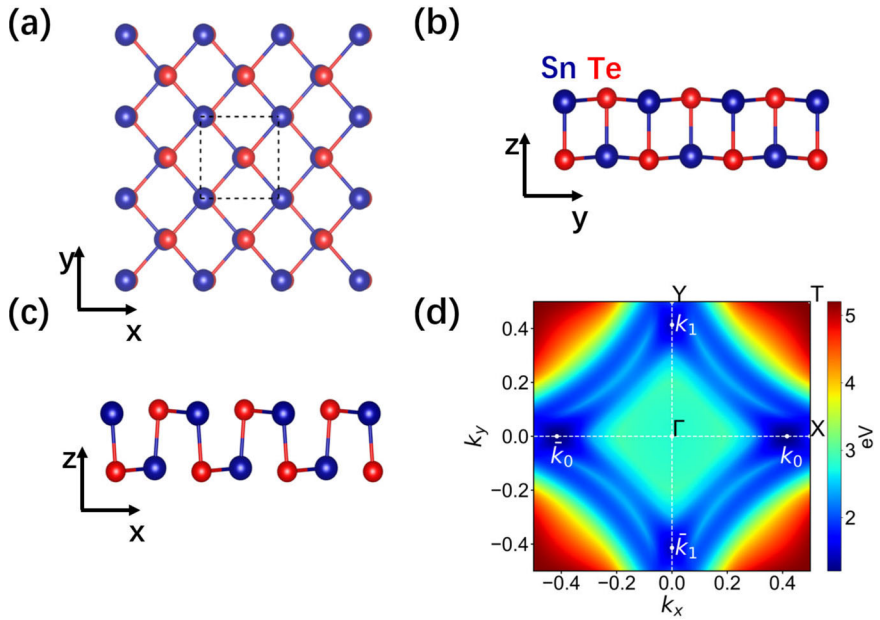

Fig. 1 Crystal structure and band gap of SnTe monolayer. a Top view, (**b**) side view along the *x* direction and (**c**) side view along the *y* direction of the crystal structure of the SnTe monolayer. The unit cell is indicated by the dashed rectangle in **a**. **d** The band gap between the lowest conduction band and the highest valence band in the Brillouin zone, where $\mathbf{k}_0$, $\bar{\mathbf{k}}_0\,\mathbf{k}_1$ and $\bar{\mathbf{k}}_1$ are the valley points.

illumination[1–3],

$$J^a = 2\sigma^{abc}(0;\omega,-\omega)E_b(\omega)E_c(-\omega), \quad (1)$$

where $\sigma^{abc}(0;\omega,-\omega)$ is the shift-current conductivity tensor, and *a* (*b*, *c*) = *x*, *y*, *z* are the crystal axes. As the SnTe monolayer is a 2D material, we do not consider the current in the *z*-direction, nor do we consider the electric field applied in the *z*-direction. Because of the mirror symmetry M_{xz} of the SnTe monolayer, only σ^{xxx}, σ^{xyy}, and $\sigma^{yxy} = \sigma^{yyx}$ are nonzero.

The first-principles calculated shift-current conductivities[3,27–29] are consistent with the above symmetry analysis. The 3D-like conductivities are obtained assuming an active single-layer thickness of 3.12 Å[28,30]. Although the results with and without SOC show some quantitative differences, the inclusion of SOC does not affect the main conclusions of this study (see Supplementary Fig. 3). Therefore, we only discuss the results without SOC here, and the analysis can be equally applied to the results with SOC.

Figure 2a shows the largest component of the shift-current conductivity tensor, σ^{yxy}, and the results for σ^{xxx} and σ^{xyy} are displayed in Supplementary Figs. 4 and 5, respectively. σ^{yxy} exhibits the highest peak at $\hbar\omega_0 = 1.21$ eV, with $\sigma^{yxy}_{3D} = 284\ \mu\text{A V}^{-2}$. This value is significantly larger than the shift-current conductivity of the known high BPVE material GeS, which is of the order of 150 μA V^{-2}, and the values of 250 μA V^{-2} reported in state-of-the-art Si-based solar cells[28,30,31].

It has been suggested that a large joint density of states (JDOS) is necessary to have a large shift current[7,8,28]. However, surprisingly, we find that the JDOS at $\hbar\omega_0 = 1.21$ eV is extremely small, as shown in Supplementary Fig. 2. Consequently, the absorption coefficient $\alpha^{[110]}$ is also very small around $\hbar\omega_0 = 1.21$ eV, as shown in Fig. 2b. It is noteworthy that the absorption coefficient α^{yy} is zero at this energy, which is strongly counterintuitive given that σ^{yxy} is enormous.

The above results have significant physical implications. We compute the Glass coefficient[1,7,9,27] $g^{abc} = \alpha^{-1}\sigma^{abc}$, and the calculated g^{yxy} is shown in Fig. 2c. At $\hbar\omega_0 = 1.21$ eV, g^{yxy} has a sharp peak due to the giant σ^{yxy} and small $\alpha^{[110]}$. The calculated Glass coefficient g^{yxy} of the SnTe monolayer is 1.8×10^{-5} cm V^{-1} (ref. [30]) at this energy, which is four orders of magnitude higher than

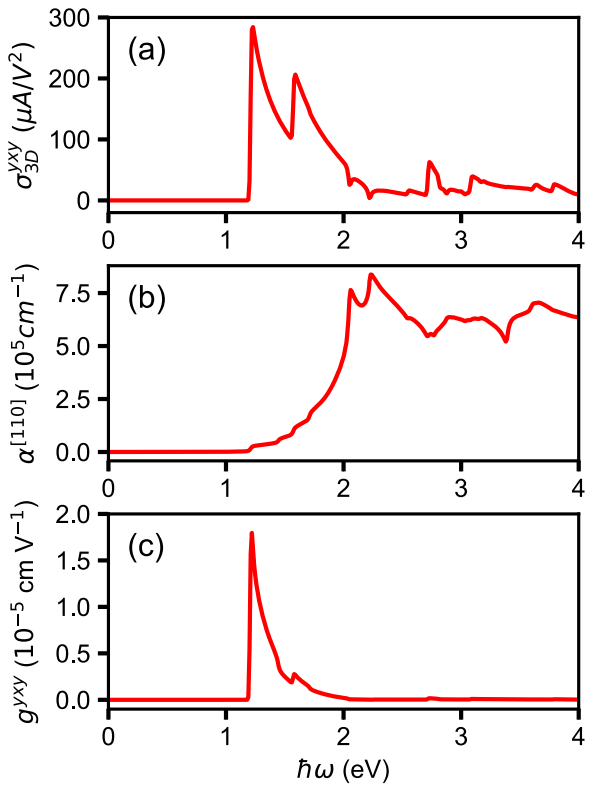

Fig. 2 Shift current spectra, absorption, and Glass coefficient of SnTe monolayer. a Shift current conductivity σ^{yxy}_{3D} of the SnTe monolayer. There are three peaks at 1.21, 1.59, and 2.73 eV, respectively. **b** The absorption coefficient $\alpha^{[110]}$ and (**c**) the Glass coefficient of the SnTe monolayer, respectively.

$g_{31} = 3 \times 10^{-9}$ cm V^{-1} of the bulk (001)-oriented $BaTiO_3$ crystal[1,5,22]. The Glass coefficient *g* plays essential roles in the shift current related physical properties. For example, the photovoltaic

field generated by the shift current[1,5] can be estimated as,

$$E_{\rm pv} \approx \frac{g}{\phi(\mu\tau)_{\rm pv}} \frac{\hbar\omega}{e}, \tag{2}$$

where ϕ is the quantum yield, $\hbar\omega$ is the incident photon energy and μ and τ are the mobility and lifetime of the carriers responsible for photoconductivity. A large value of the Glass coefficient g can result in a significant increase in the photovoltaic field $E_{\rm pv}$ because, in such cases, the shift current dominates over the "leaking current" caused by photoconductivity. The photovoltaic power conversion efficiency is also closely related to the Glass coefficient[1], where the maximum efficiency is $\eta_{\max} = gE_{\rm pv}/4$.

To experimentally explore this giant shift current effect, we could apply light with an electric field polarized along the [110] direction, and measure the resulting shift current along the y direction, which gives,

$$J^y = 2\sigma^{yxy} E_x(\omega) E_y(-\omega). \tag{3}$$

It has been shown that strong excitonic effects may further enhance the shift-current effects in 2D materials[32,33]. To enable the unambiguous detection of the shift-vector-induced effects while minimizing potential interference from other effects (e.g., the exciton effect), one may use laser energy that matches the band-to-band transition energy, which is typically much higher than the exciton absorption energy. Investigating how many-body effects change the shift-current in SnTe will be an interesting topic for future investigation.

DISCUSSION

It is particularly interesting and important to explore the underlying mechanism of the giant shift-current conductivity and Glass coefficient in the SnTe monolayer. The shift-current tensor is given by[3],

$$\sigma^{abc}(0;\omega,-\omega) = \frac{\pi e^3}{\hbar^2}\int \frac{d\mathbf{k}}{8\pi^3} \sum\nolimits_{n,m} f_{nm} {\rm Im}\left[I^{abc}_{mn} + I^{acb}_{mn}\right] \delta(\omega_{mn} - \omega), \tag{4}$$

where $f_{nm} = f_n - f_m$ and $\hbar\omega_{nm} = E_n - E_m$ are differences between Fermi occupation factors and band energies, respectively. $I^{abc}_{mn} = r^b_{mn} r^c_{nm;a}$, where r^a_{nm} is the inter-band dipole matrix, and $r^b_{nm;a}$ is the generalized derivative of the dipole matrix, i.e.,

$$r^a_{nm} = (1 - \delta_{nm}) A^a_{nm}, \tag{5}$$

$$r^a_{nm;b} = \partial_b r^a_{nm} - i\left(A^b_{nn} - A^b_{mm}\right) r^a_{nm}. \tag{6}$$

Here, A^a_{nm} is the non-Abelian Berry connection. Although r^a_{nm} and $r^b_{nm;a}$ are gauge dependent, their norm $|r^a_{nm}|$ and $|r^b_{nm;a}|$, as well as I^{abc}_{mn} are gauge invariant[28]. Note that r^a_{nm} and $r^b_{nm;a}$ and I^{abc}_{mn} are all $\mathbf{k}$ dependent, but we drop the k index here for simplicity.

We calculate $\sum_{n,m} f_{nm} {\rm Im}\left[I^{yxy}_{mn} + I^{yyx}_{mn}\right] \delta(\omega_{mn} - \omega_0)$ in the first BZ at $\hbar\omega_0 = 1.21$ eV. We find that the contribution only arises from the transition between the highest valence (v) band and the lowest conduction (c) band near the valley points $\mathbf{k}_0$ and $\bar{\mathbf{k}}_0$ as shown in Supplementary Fig. 6a.

Because only the valley points contribute to the optical transitions at $\hbar\omega_0$, the corresponding JDOS and linear absorption coefficient is very small. Furthermore, as shown in Supplementary Fig. 6b, $I_{vc} = {\rm Im}\left[I^{yxy}_{vc} + I^{yyx}_{vc}\right]$, has a bright spot at $\mathbf{k}_0$, which gives rise to the giant shift-current conductivity.

Figure 3a shows the norm of r^x_{vc} and r^y_{vc} along k_y passing through $\mathbf{k}_0$, represented by the red and blue solid lines, respectively. We observe that $|r^x_{vc}|$ reaches a maximum at $k_y = 0$, whereas $|r^y_{vc}| = 0$ at $\mathbf{k}_0$ due to the mirror symmetry M_{xz}. However, as seen from Fig. 3a, $|r^y_{vc}|$ changes rapidly along k_y around $\mathbf{k}_0$. One may speculate that r^y_{vc} may have a large partial derivative in Eq. (6) along k_y at the valley point. Indeed, as shown in Fig. 3b, $|r^y_{cv;y}|$

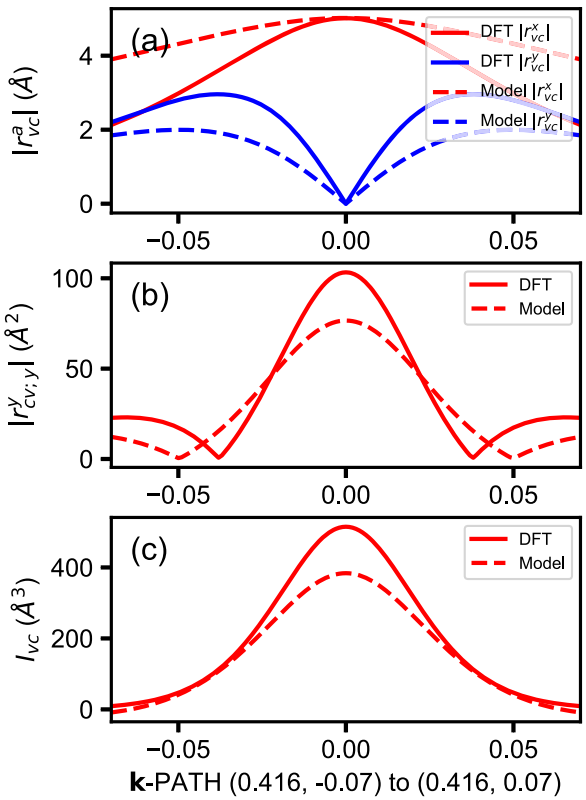

Fig. 3 DFT and model analysis of dipole matrix, its generalized derivatives, and shift current contribution along k_y. a The norm of dipole matrix r^x_{vc} and r^y_{vc} along k_y, where v and c are highest valence band and lowest conduction band, respectively. **b** The norm of the generalized derivative of dipole matrix, $r^y_{cv;y}$, along k_y. **c** The $I_{vc} = {\rm Im}\left[I^{yxy}_{vc} + I^{yyx}_{vc}\right]$ along k_y. The results obtained from DFT and model calculations are shown in solid and dashed lines, respectively.

exhibits a peak at $\mathbf{k}_0$. We plot I_{vc} in Fig. 3c. Interestingly, we find that $I_{vc} \approx |r^x_{vc}||r^y_{cv;y}|$ around $\mathbf{k}_0$. Both r^x_{vc} and $r^y_{cv;y}$ reach their maximum values at $\mathbf{k}_0$, leading to the giant I_{vc}.

To gain a deeper insight into the physics involved, we construct a minimal three-band model around the valley point $\mathbf{k}_0$,

$$H(\mathbf{k}) = H_0 + \mathbb{A}\delta k_x + \mathbb{B}\delta k_y + \mathbb{C}\delta k_x^2 + \mathbb{D}\delta k_x \delta k_y + \mathbb{E}\delta k_y^2, \tag{7}$$

up to the quadratic terms of $\delta\mathbf{k}$, where $\delta\mathbf{k} = \mathbf{k} - \mathbf{k}_0$. More specifically, $\delta k_x = k_x - 0.416$, $\delta k_y = k_y$. We therefore do not distinguish k_y and δk_y below. In the model, the 1st band is the highest valence band, whereas the 2nd band and 3rd band correspond to the lowest two conduction bands in the DFT calculations. We fit the Hamiltonian matrix $H(\mathbf{k})$ and velocity matrix $v_{mn}(\mathbf{k})$ from DFT calculations around $\mathbf{k}_0$. The fitted parameters of the model are given in Supplementary Information.

We first (numerically) calculate $|r^x_{12}|$, $|r^y_{12;y}|$, and I_{12} of the three-band model, and the results are compared with those from DFT calculations in Fig. 3a–c, respectively. The three-band model can reproduce the results of the DFT calculations semi-quantitatively, and the discrepancies can be attributed to the omission of other bands in the model.

Around $\mathbf{k}_0$, the three-band model can be analytically solved using second order perturbation theory, and consequently r^a_{nm} and $r^a_{nm;b}$ can also be calculated analytically. Especially, at $\mathbf{k}_0$ we have $v^x_{nm}(\mathbf{k}_0) = \mathbb{A}_{nm}$ and $v^y_{nm}(\mathbf{k}_0) = \mathbb{B}_{nm}$, therefore by using Eq.

(18) in METHOD section, we have

$$r^x_{nm}(\mathbf{k_0}) = \frac{\mathbb{A}_{nm}}{i\omega_{nm}}, \quad r^y_{nm}(\mathbf{k_0}) = \frac{\mathbb{B}_{nm}}{i\omega_{nm}}. \tag{8}$$

Because $\mathbb{A}_{12}\neq 0$, and $\mathbb{B}_{12} = 0$, which is actually imposed by the mirror symmetry, we have $r^x_{12}(\mathbf{k}_0)\neq 0$, but $r^y_{12}(\mathbf{k}_0) = 0$. This means that the linear (or direct) optical transition between the 1st and 2nd bands along k_y is forbidden. Similarly we calculate the $r^b_{nm;a}$ of the valley point $\mathbf{k}_0$, and we have,

$$r^y_{21;y}(\mathbf{k_0}) = \frac{i}{\omega_{21}}\left[\mathbb{B}_{23}\mathbb{B}_{31}\left(\frac{1}{\omega_{31}}+\frac{1}{\omega_{32}}\right) - 2\mathbb{E}_{21}\right]. \tag{9}$$

In the model, the value of $r^y_{21,y}$ (and therefore I^{yxy}_{12}) depends mainly on the virtual transitions $\mathbb{B}_{23}\mathbb{B}_{31}$, which corresponding to the last term of Eq. (19) in METHOD section. The first term of Eq. (19) vanishes, because $\mathbb{B}_{12} = 0$. This is remarkable that the linear (direct) optical transition between the 1st band and the 2nd band in the y direction is forbidden, but the nonlinear transition may occur because both the 1st band and 2nd band have strong coupling with the 3rd-band, which leads to the giant shift-current effect. This effect is quite different from that of the two-band models for Weyl semimetals[17].

The giant shift-current effects in SnTe have even more profound origins. An alternative expression for the shift-current conductivity is written as[17],

$$\sigma^{yxy} = -\frac{\pi e^3}{\hbar^2}\int_{\mathbf{k}}\sum_{n,m} f_{nm}\left(R^y_{mn;y} - R^x_{nm;y}\right) r^x_{nm} r^y_{mn} \\ \delta(\omega_{mn} - \omega), \tag{10}$$

where,

$$R^b_{mn;a} = i\partial_a \ln r^b_{mn} + A^a_{mm} - A^a_{nn}, \tag{11}$$

is known as the shift vector, which characterizes the displacement of electrons in real space during the inter-band transition[1,34,35]. The shift vector is a gauge invariant quantity and can be viewed as a quantum geometric potential[36]. According to the perturbation theory, near $\mathbf{k}_0$, $r^y_{12}(\mathbf{k}) = f_4\, k_y + f_5\, \delta k_x k_y$, where f_4 and f_5 are constants. In the model, $A^a_{11}(\mathbf{k}_0) = 0$ and $A^a_{22}(\mathbf{k}_0) = 0$ at $\mathbf{k}_0$, and both are small around $\mathbf{k}_0$. We can therefore neglect them in the following calculations. As $\mathbf{k}$ approaches $\mathbf{k}_0$ along k_y, i.e., $\delta k_x = 0$, we have,

$$R^y_{12;y} = i\partial_y \ln(f_4\, k_y) = \frac{i}{k_y}, \tag{12}$$

i.e., $R^y_{12;y}$ is purely imaginary and goes to infinity. Therefore, $\mathbf{k}_0$ is a singular point for the shift vector $R^y_{12;y}$, which is a monopole in k-space. When k_y is approaching zero, r^y_{12} is also approaching zero as discussed in previous sections, and $R^x_{21;y} r^x_{21} r^y_{12}$ vanishes, but $R^y_{12;y} r^x_{21} r^y_{12}$ is still finite (actually very large) and purely real (Fig. 3). The introduction of SOC will not break the mirror symmetry, and therefore the above analyses remain valid. The shift vector would diverge at the valley points, as evidenced by Supplementary Fig. 3. Even after the introduction of SOC, the Glass coefficient at the valley points remains significantly large.

The shift vectors also play important roles in second harmonic generation[17,37,38]. It is therefore expected that the SnTe monolayer would have non-trivial second harmonic responses. The divergence of the shift vector at the so-called "optical zero" was discussed in ref. [39]. However, the relation between the giant shift current and the divergent shift vector has not been revealed.

Very recently, nonlinear optical transitions have been related to the Riemannian geometry of the energy bands[17,40]. We may define the quantum geometric tensor between two bands m and n,

$$Q^{mn}_{ba} = r^b_{nm} r^a_{mn} \equiv g^{mn}_{ba} - \frac{i}{2} F^{mn}_{ba}, \quad a, b = x, y, z \tag{13}$$

where g^{mn}_{ba} is the band-resolved quantum metric, F^{mn}_{ba} is the band-resolved Berry curvature, and the two geometric quantities are related to U(1) quantum metric and Berry curvature as $g^n_{ba} = \sum_{m\neq n} g^{mn}_{ba}$ and $\Omega^n_c = \sum_{m\neq n}\epsilon_{cba} F^{mn}_{ba}/2$[41,42].

In our case, we consider the transition between the 1st band and the 2nd band, and the quantum geometric tensor of the two bands is given by $Q^{12}_{xy} = r^x_{12} r^y_{21}$. We have $Q^{12}_{xy}(\mathbf{k_0}) = 0$ because $r^y_{21}(\mathbf{k_0}) = 0$. However, we show that the partial derivative of the imaginary part of Q^{12}_{xy} is related to I^{yxy}_{12}, i.e.,

$$\mathrm{Im}\left[I^{yxy}_{12}(\mathbf{k_0})\right] = \partial_y \mathrm{Im}\left[Q^{12}_{xy}\right]\Big|_{\mathbf{k}=\mathbf{k}_0} = -\frac{1}{2}\partial_y F^{12}_{xy}\Big|_{\mathbf{k}=\mathbf{k}_0}. \tag{14}$$

Fig. 4a illustrates the distribution of $\mathrm{Im}[Q^{12}_{xy}]$ near $\mathbf{k}_0$ and its derivative with respect to k_y is shown in Fig. 4b. $\mathrm{Im}[Q^{12}_{xy}]$ has a maximum (minimum) at $\delta k_y = 0.05$ ($\delta k_y = -0.05$) and $\delta k_x = 0$, which is very similar to the Berry curvature distribution in Fig. 2a of ref. [26]. Furthermore, $\mathrm{Im}[Q^{12}_{xy}]$ changes rapidly around $\delta k_y = 0$, and as a consequence, $\mathrm{Im}\left[I^{yxy}_{12}(\mathbf{k}_0)\right]$ has a maximum at $\mathbf{k}_0$, which is consistent with that from direct calculations.

We have demonstrated that the giant shift-current and Glass coefficient are directly induced by the divergent shift-vector near the valley points. Our three-band model has revealed several crucial requirements for achieving these effects. Firstly, the band structure should possess valley points located on a k-line with mirror symmetry, ensuring the divergence of the shift vector. Additionally,

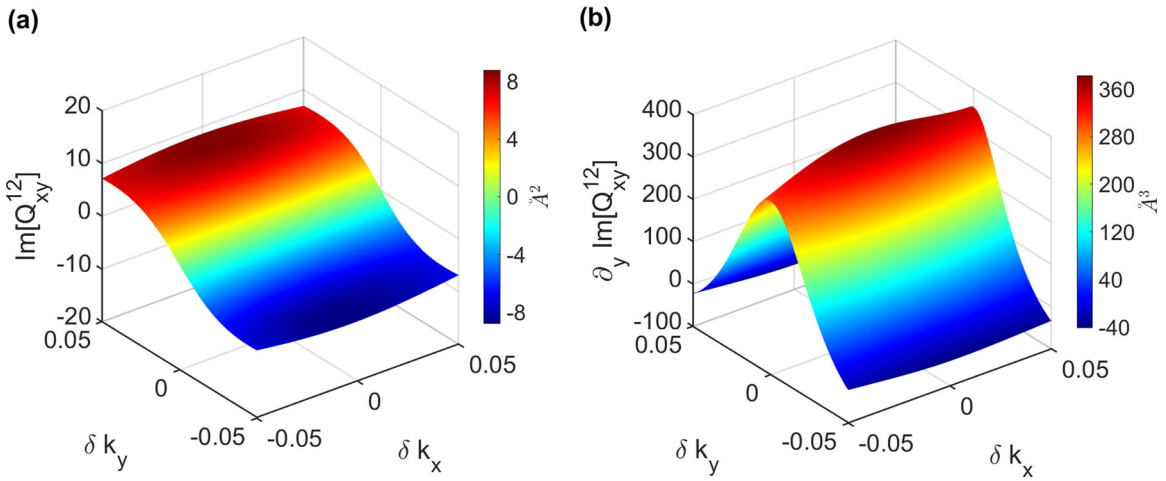

Fig. 4 Quantum geometric tensor near valley point $\mathbf{k_0}$. The distributions of (**a**) $\mathrm{Im}\left[Q^{12}_{xy}\right]$ and (**b**) $\partial_y \mathrm{Im}\left[Q^{12}_{xy}\right]$ around the valley point $\mathbf{k}_0$.

the structure should break the inversion symmetry within the mirror plane to have non-zero r^x_{nm}. Notably, there are numerous materials that meet these conditions, such as the MX family, including GeS, GeSe, GeTe, SnS, SnSe[30,43], which exhibit similar properties.

In summary, our study unveils a significant shift current effect and an extremely large Glass coefficient in the ferroelectric SnTe monolayer. These effects stem from the divergence of the shift-vector near valley points, highlighting the influence of band geometry on nonlinear optical transitions. These findings present remarkable evidence of measurable physical effects arising from shift-vector divergence in semiconductors. They also offer valuable guidance in the search for materials with significant shift current effects, holding promise for their application in photoelectric devices.

METHODS

Self-consistent calculations

The first-principles calculations are carried out with the Atomic orbital Based Ab-initio Computation at UStc (ABACUS) code[44,45]. The Heyd-Scuseria-Ernzerhof (HSE) exchange-correlation functional[46] is used. The ABACUS code is developed to perform large-scale density functional theory calculations based on numerical atomic orbitals (NAO)[44,47] and supports for large-scale HSE calculations[48–50]. The optimized norm-conserving Vanderbilt (ONCV)[51] fully relativistic pseudopotentials[52] from the PseudoDojo library[53] are used. The valence electrons for Sn, Te are $4d^{10}5s^25p^2$, and $4d^{10}5s^25p^4$, and the NAO bases for Sn and Te are 2s2p2d1f and 2s2p2d1f, respectively[47].

In the self-consistent and band structure calculations, the energy cut-off for the wave functions is set to 150 Ry. The Brillouin zone is sampled using a Γ-centered $16\times16\times1$ k-point mesh. The structure is fully optimized until all forces are less than 1 meV Å^{-1}.

Shift-current conductivity

After the self-consistent calculations, the tight-binding Hamiltonian,

$$H_{\mu\nu}(\mathbf{R}) = \langle \mathbf{0}\mu|H|\mathbf{R}\nu\rangle, \tag{15}$$

the overlap matrices,

$$S_{\mu\nu}(\mathbf{R}) = \langle \mathbf{0}\mu|\mathbf{R}\nu\rangle, \tag{16}$$

and the dipole matrices (between the NAOs),

$$\mathbf{r}_{\mu\nu}(\mathbf{R}) = \langle \mathbf{0}\mu|\mathbf{r}|\mathbf{R}\nu\rangle, \tag{17}$$

in the NAO bases are generated, where $|\mathbf{R}\nu\rangle = \phi_\nu(\mathbf{r}-\tau_\nu-\mathbf{R})$ is the ν-th NAO in the $\mathbf{R}$-th cell, and τ_ν is the center of the ν-th NAO in the unit cell.

The dipole matrix r^a_{nm} and its generalized derivative $r^a_{nm;b}$ in the shift current Eqs. (5)–(6) are calculated as follows[3,8,28] (here we drop the k index for simplicity),

$$r^a_{nm} = \frac{v^a_{nm}}{i\omega_{nm}} \quad (m\neq n), \tag{18}$$

and

$$r^a_{nm;b} = \frac{i}{\omega_{nm}}\Big[\frac{v^a_{nm}\Delta^b_{nm}+v^b_{nm}\Delta^a_{nm}}{\omega_{nm}} - w^{ab}_{nm} + \sum_{p\neq n,m}\Big(\frac{v^a_{np}v^b_{pm}}{\omega_{pm}} - \frac{v^b_{np}v^a_{pm}}{\omega_{np}}\Big)\Big] \quad (m\neq n), \tag{19}$$

where,

$$\begin{aligned} v^a_{nm} &= \tfrac{1}{\hbar}\langle u_{n\mathbf{k}}|\partial_a H(\mathbf{k})|u_{m\mathbf{k}}\rangle,\\ \omega_{nm} &= E_n - E_m,\\ \Delta^a_{nm} &= \partial_a\omega_{nm} = v^a_{nn} - v^a_{mm},\\ w^{ab}_{nm} &= \tfrac{1}{\hbar}\langle u_{n\mathbf{k}}|\partial^2_{ab}H(\mathbf{k})|u_{m\mathbf{k}}\rangle. \end{aligned} \tag{20}$$

The velocity matrix elements v^a_{nm} are calculated by the ab initio tight-binding Hamiltonian Eqs. (15)–(17)[54,55]. The calculated shift-current conductivities and Glass coefficients are converted to effective 3D values, following refs. [28,30]. More details can be found in Supplementary Information.

The band structures and the optical properties, such as the shift current are calculated using the tight-binding Hamiltonian implemented in the PY-ATB code[56].

DATA AVAILABILITY

All data generated and/or analyzed during this study are included in this article.

CODE AVAILABILITY

The ABACUS code is an open source DFT code under the GPL 3.0 licence, which is available from http://abacus.ustc.edu.cn. The Py-ATB code, also under the GPL 3.0 licence, can be downloaded from https://github.com/pyatb.

Received: 12 September 2023; Accepted: 18 January 2024;
Published online: 29 January 2024

REFERENCES

1. Sturman, B. I. & Fridkin, V. M. *The Photovoltaic and Photorefractive Effects in Noncentrosymmetric Materials* (Gordon and Breach Science Publishers, 1992).
2. von Baltz, R. & Kraut, W. Theory of the bulk photovoltaic effect in pure crystals. *Phys. Rev. B* **23**, 5590–5596 (1981).
3. Sipe, J. E. & Shkrebtii, A. I. Second-order optical response in semiconductors. *Phys. Rev. B* **61**, 5337–5352 (2000).
4. Shockley, W. & Queisser, H. J. Detailed balance limit of efficiency of p-n junction solar cells. *J. Appl. Phys.* **32**, 510–519 (1961).
5. Spanier, J. E. et al. Power conversion efficiency exceeding the shockley-queisser limit in a ferroelectric insulator. *Nat. Photon.* **10**, 611–616 (2016).
6. Nastos, F. & Sipe, J. E. Optical rectification and current injection in unbiased semiconductors. *Phys. Rev. B* **82**, 235204 (2010).
7. Tan, L. Z. et al. Shift current bulk photovoltaic effect in polar materials-hybrid and oxide perovskites and beyond. *NPJ Comput. Mater.* **2**, 1–12 (2016).
8. Cook, A. M., M Fregoso, B., De Juan, F., Coh, S. & Moore, J. E. Design principles for shift current photovoltaics. *Nat. Commun.* **8**, 1–9 (2017).
9. Glass, A. M., von der Linde, D. & Negran, T. J. High-voltage bulk photovoltaic effect and the photorefractive process in $LiNbO_3$. *Appl. Phys. Lett.* **25**, 233–235 (1974).
10. Dalba, G., Soldo, Y., Rocca, F., Fridkin, V. M. & Sainctavit, P. Giant bulk photovoltaic effect under linearly polarized x-ray synchrotron radiation. *Phys. Rev. Lett.* **74**, 988–991 (1995).
11. Yang, S. et al. Above-bandgap voltages from ferroelectric photovoltaic devices. *Nat. Nanotechnol.* **5**, 143–147 (2010).
12. Alexe, M. & Hesse, D. Tip-enhanced photovoltaic effects in bismuth ferrite. *Nat. Commun.* **2**, 1–5 (2011).
13. Bhatnagar, A. et al. Role of domain walls in the abnormal photovoltaic effect in $BiFeO_3$. *Nat. Commun.* **4**, 1–8 (2013).
14. Ogawa, N., Sotome, M., Kaneko, Y., Ogino, M. & Tokura, Y. Shift current in the ferroelectric semiconductor SbSI. *Phys. Rev. B* **96**, 241203(R) (2017).
15. Osterhoudt, G. B. et al. Colossal mid-infrared bulk photovoltaic effect in a type-i weyl semimetal. *Nat. Mater.* **18**, 471–475 (2019).
16. Ma, J. et al. Nonlinear photoresponse of type-ii weyl semimetals. *Nat. Mater.* **18**, 476–481 (2019).
17. Ahn, J., Guo, G.-Y. & Nagaosa, N. Low-frequency divergence and quantum geometry of the bulk photovoltaic effect in topological semimetals. *Phys. Rev. X* **10**, 041041 (2020).
18. Cheng, M., Zhu, Z.-Z. & Guo, G.-Y. Strong bulk photovoltaic effect and second-harmonic generation in two-dimensional selenium and tellurium. *Phys. Rev. B* **103**, 245415 (2021).
19. Gudelli, V. K. & Guo, G.-Y. Large bulk photovoltaic effect and second-harmonic generation in few-layer pentagonal semiconductors PdS_2 and $PdSe_2$. *N. J. Phys.* **23**, 093028 (2021).
20. Lihm, J.-M. & Park, C.-H. Comprehensive theory of second-order spin photocurrents. *Phys. Rev. B* **105**, 045201 (2022).
21. Chang, K. et al. Discovery of robust in-plane ferroelectricity in atomic-thick snte. *Science* **353**, 274–278 (2016).
22. Zenkevich, A. et al. Giant bulk photovoltaic effect in thin ferroelectric $BaTiO_3$ films. *Phys. Rev. B* **90**, 161409(R) (2014).

23. Wan, W., Liu, C., Xiao, W. & Yao, Y. Promising ferroelectricity in 2d group iv tellurides: a first-principles study. *Appl. Phys. Lett.* **111**, 132904 (2017).
24. Chang, K. et al. Enhanced spontaneous polarization in ultrathin snte films with layered antipolar structure. *Adv. Mater.* **31**, 1804428 (2019).
25. Absor, M. A. U. & Ishii, F. Intrinsic persistent spin helix state in two-dimensional group-iv monochalcogenide *MX* monolayers (M = Sn or Ge and X = S, Se, or Te). *Phys. Rev. B* **100**, 115104 (2019).
26. Kim, J. et al. Prediction of ferroelectricity-driven berry curvature enabling charge- and spin-controllable photocurrent in tin telluride monolayers. *Nat. Commun.* **10**, 1–9 (2019).
27. Young, S. M. & Rappe, A. M. First principles calculation of the shift current photovoltaic effect in ferroelectrics. *Phys. Rev. Lett.* **109**, 116601 (2012).
28. Ibañez Azpiroz, J., Tsirkin, S. S. & Souza, I. Ab initio calculation of the shift photocurrent by wannier interpolation. *Phys. Rev. B* **97**, 245143 (2018).
29. Wang, C. et al. First-principles calculation of optical responses based on non-orthogonal localized orbitals. *N. J. Phys.* **21**, 093001 (2019).
30. Rangel, T. et al. Large bulk photovoltaic effect and spontaneous polarization of single-layer monochalcogenides. *Phys. Rev. Lett.* **119**, 067402 (2017).
31. Pagliaro, M., Ciriminna, R. & Palmisano, G. Flexible solar cells. *ChemSusChem* **1**, 880–891 (2008).
32. Chan, Y.-H., Qiu, D. Y., da Jornada, F. H. & Louie, S. G. Giant exciton-enhanced shift currents and direct current conduction with subbandgap photo excitations produced by many-electron interactions. *Proc. Natl Acad. Sci. USA* **118**, e1906938118 (2021).
33. Gao, S., Liang, Y., Spataru, C. D. & Yang, L. Dynamical excitonic effects in doped two-dimensional semiconductors. *Nano Lett.* **16**, 5568–5573 (2016).
34. Sturman, B. I. Ballistic and shift currents in the bulk photovoltaic effect theory. *Phys.-Usp.* **63**, 407 (2020).
35. Jiang, J. et al. Flexo-photovoltaic effect in MoS_2. *Nat. Nanotechnol.* **16**, 894–901 (2021).
36. Wu, J.-d, Zhao, M.-s, Chen, J.-l & Zhang, Y.-d Adiabatic condition and quantum geometric potential. *Phys. Rev. A* **77**, 062114 (2008).
37. Morimoto, T. & Nagaosa, N. Topological nature of nonlinear optical effects in solids. *Sci. Adv.* **2**, e1501524 (2016).
38. Nagaosa, N. & Morimoto, T. Concept of quantum geometry in optoelectronic processes in solids: application to solar cells. *Adv. Mater.* **29**, 1603345 (2017).
39. Fregoso, B. M., Morimoto, T. & Moore, J. E. Quantitative relationship between polarization differences and the zone-averaged shift photocurrent. *Phys. Rev. B* **96**, 075421 (2017).
40. Ahn, J., Guo, G.-Y., Nagaosa, N. & Vishwanath, A. Riemannian geometry of resonant optical responses. *Nat. Phys.* **18**, 290–295 (2022).
41. Gao, Y., Zhang, Y. & Xiao, D. Tunable layer circular photogalvanic effect in twisted bilayers. *Phys. Rev. Lett.* **124**, 077401 (2020).
42. Watanabe, H. & Yanase, Y. Chiral photocurrent in parity-violating magnet and enhanced response in topological antiferromagnet. *Phys. Rev. X* **11**, 011001 (2021).
43. Kaner, N. T. et al. Enhanced shift currents in monolayer 2d ges and sns by strain-induced band gap engineering. *ACS Omega* **5**, 17207–17214 (2020).
44. Chen, M., Guo, G.-C. & He, L. Systematically improvable optimized atomic basis sets forab initiocalculations. *J. Phys. Condens. Matter* **22**, 445501 (2010).
45. Li, P. et al. Large-scale ab initio simulations based on systematically improvable atomic basis. *Comput. Mater. Sci.* **112**, 503–517 (2016).
46. Heyd, J., Scuseria, G. E. & Ernzerhof, M. Hybrid functionals based on a screened coulomb potential. *J. Chem. Phys.* **118**, 8207–8215 (2003).
47. Lin, P., Ren, X. & He, L. Strategy for constructing compact numerical atomic orbital basis sets by incorporating the gradients of reference wavefunctions. *Phys. Rev. B* **103**, 235131 (2021).
48. Lin, P., Ren, X. & He, L. Accuracy of localized resolution of the identity in periodic hybrid functional calculations with numerical atomic orbitals. *J. Phys. Chem. Lett.* **11**, 3082–3088 (2020).
49. Lin, P., Ren, X. & He, L. Efficient hybrid density functional calculations for large periodic systems using numerical atomic orbitals. *J. Chem. Theory Comput.* **17**, 222–239 (2021).
50. Ji, Y., Lin, P., Ren, X. & He, L. Reproducibility of hybrid density functional calculations for equation-of-state properties and band gaps. *J. Phys. Chem. A* **126**, 5924–5931 (2022).
51. Hamann, D. R. Optimized norm-conserving vanderbilt pseudopotentials. *Phys. Rev. B* **88**, 085117 (2013).
52. Theurich, G. & Hill, N. A. Self-consistent treatment of spin-orbit coupling in solids using relativistic fully separable ab initio pseudopotentials. *Phys. Rev. B* **64**, 073106 (2001).
53. van Setten, M. et al. The pseudodojo: Training and grading a 85 element optimized norm-conserving pseudopotential table. *Comput Phys. Commun.* **226**, 39–54 (2018).
54. Lee, C.-C., Lee, Y.-T., Fukuda, M. & Ozaki, T. Tight-binding calculations of optical matrix elements for conductivity using nonorthogonal atomic orbitals: Anomalous hall conductivity in bcc fe. *Phys. Rev. B* **98**, 115115 (2018).
55. Jin, G., Zheng, D. & He, L. Calculation of berry curvature using non-orthogonal atomic orbitals. *J. Phys. Condens. Matter* **33**, 325503 (2021).
56. Jin, G., Pang, H., Ji, Y., Dai, Z. & He, L. Pyatb: An efficient python package for electronic structure calculations using ab initio tight-binding model. *Comput Phys. Commun.* **291**, 108844 (2023).

ACKNOWLEDGEMENTS

This work was funded by the National Natural Science Foundation of China, Grant Number 12134012, and the Innovation Program for Quantum Science and Technology, Grant Number 2021ZD0301200. The numerical calculations were performed on the USTC HPC facilities.

AUTHOR CONTRIBUTIONS

L. He conducted the project. G. Jin developed the computer code and performed the calculations under the supervision of L. He. Both authors analyzed the results and wrote the manuscript.

COMPETING INTERESTS

The authors declare no competing interests.

ADDITIONAL INFORMATION

Supplementary information The online version contains supplementary material available at https://doi.org/10.1038/s41524-024-01213-w.

Correspondence and requests for materials should be addressed to Lixin He.

Reprints and permission information is available at http://www.nature.com/reprints

Publisher's note Springer Nature remains neutral with regard to jurisdictional claims in published maps and institutional affiliations.